Heliyon 9 (2023) e21270

Contents lists available at ScienceDirect

Heliyon

journal homepage: www.cell.com/heliyon

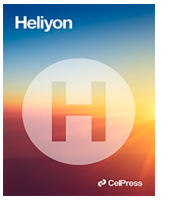

Sn-doped BiOCl for photoelectrochemical activities and photocatalytic dye degradation under visible light

Asyiqin Zulkiflee [a], Mohammad Mansoob Khan [a,*], Abuzar Khan [b], Mohd Yusuf Khan [b], Hatim Dafalla Mohamed Dafalla [c], Mohammad Hilni Harunsani [a]

[a] Chemical Sciences, Faculty of Science, Universiti Brunei Darussalam, Jalan Tungku Link, Gadong, BE 1410, Brunei Darussalam
[b] Interdisciplinary Research Center for Hydrogen and Energy Storage, King Fahd University of Petroleum & Minerals (KFUPM), Dhahran, 31261, Saudi Arabia
[c] Core Research Facilities, King Fahd University of Petroleum and Minerals, Dhahran, 31261, Saudi Arabia

ARTICLE INFO

Keywords:
Bismuth oxychloride
BiOCl
Sn-doped BiOCl
Visible light
Rhodamine B
Photocatalysis

ABSTRACT

In this work, bismuth oxychloride (BiOCl) and Sn-doped BiOCl (SBCl) with improved visible light photocatalytic activity were synthesized via the co-precipitation method. The XRD analysis determined the tetragonal phase of BiOCl, 1 %, 5 %, and 10 % SBCl. The crystallite sizes were in the range of 20–34 nm. These results confirmed that the Sn ion was successfully incorporated into the BiOCl lattice. This was further confirmed by FT-IR and Raman analysis. The optical properties, such as the band gap energy, were studied using UV–vis DRS. It was found that doping BiOCl with Sn has a minor effect on the band gap tuning. BET shows that the SBCl samples have acquired a larger specific surface area (14.66–42.20 m^2/g) than BiOCl (13.49 m^2/g). The photocatalytic performance showed that SBCl samples have higher photocatalytic activity than BiOCl in degrading Rhodamine B (RhB) dye under visible light irradiation. Among the SBCl samples, 5 % SBCl exhibited the highest photocatalytic efficiency which degraded 91.2 % of the RhB dye in 60 min. Moreover, the photoelectrochemical activities of the as-synthesized BiOCl and SBCl were investigated using linear sweep voltammetry (LSV) and electrochemical impedance spectroscopy (EIS) in the dark and under visible light irradiation. Both studies showed that SBCl exhibits enhanced photoelectrochemical activities than BiOCl. Hence, it can be suggested that SBCl possesses visible light active properties and can be potentially used as a photocatalyst and photoelectrode material.

1. Introduction

Numerous types of semiconductor photocatalysts, such as TiO_2, ZnO, CdS, and MoS_2 have been developed for water splitting and removing organic contaminants using solar energy [1,2]. TiO_2 is a well-known standard model photocatalyst for understanding photocatalysis. This is due to their biocompatibility, excellent stability under various conditions, and capacity to produce charge carriers when excited with the appropriate type and intensity of light [1]. However, TiO_2 is only active in UV light because of its wide band gap (~3.2 eV) [3,4]. Therefore, the design of visible-light-active photocatalysts is essential for the effective use of solar energy. Visible light is considered to be a safe, economical, environmentally friendly, and sustainable energy resource when used in

* Corresponding author.
E-mail addresses: mmansoobkhan@yahoo.com, mansoob.khan@ubd.edu.bn (M.M. Khan).

https://doi.org/10.1016/j.heliyon.2023.e21270
Received 22 July 2023; Received in revised form 12 October 2023; Accepted 18 October 2023
Available online 27 October 2023
2405-8440/© 2023 The Authors. Published by Elsevier Ltd. This is an open access article under the CC BY-NC-ND license (http://creativecommons.org/licenses/by-nc-nd/4.0/).

photocatalytic processes [5,6]. Numerous compounds have been considered and studied as potential visible light-driven materials. For instance, chalcogenide-based materials are known as one of the visible light active materials [7]. This is due to its narrow bandgap energy, capability to harvest visible light, and several applications including solar energy utilization, visible light photocatalysis, visible light-assisted water splitting, and removal of harmful contaminants [2,7]. Various studies were conducted with the aim of degrading hazardous water pollutants using an efficient, stable, and visible light-responsive photocatalyst. Currently, visible light-active photocatalysts such as bismuth-based materials are being studied for wastewater treatment [8].

Recently, the high photocatalytic activities of bismuth oxyhalides (BiOX (X = Cl, Br, and I) have been presented as a novel family of promising visible-light-active photocatalysts, which have attracted the attention of many scientific researchers [9–11]. Among them, bismuth oxychloride (BiOCl) is a non-toxic, cost-effective, and eco-friendly photocatalyst [12]. BiOCl has a distinctive layered structure consisting of a $[Bi_2O_2]^{2+}$ layer with two $[Cl]^-$ layers sandwiched between one another [13,14]. The static electric field adjacent to $[Bi_2O_2]^{2+}$ and $[Cl]^-$ layers causes a polarity in electronegativities between layers which can lead to the separation of electron-hole pairs. Therefore, it helps to enhance the photocatalytic performance [13,15,16]. Additionally, the unique layered structure contributes to improving the separation efficiency between photoinduced electrons and holes, which results in excellent photoelectrochemical abilities [17].

Different methods are reported to increase the capacity of semiconductor photocatalysts to effectively absorb light, including doping, composites, etc. [9,18–22]. Doping is one of the promising modification strategies to increase photocatalytic activity. For instance, Liu et al. prepared Co-doped BiOCl and degraded 98.9 % of Rhodamine B dye (RhB) which was 1.43 times greater than BiOCl under visible light irradiation [19]. In another study, Zr-doped BiOCl was reported to have greater photocatalytic activity than BiOCl, which was 3 times more effective at degrading RhB dye [22]. Furthermore, Zhong et al. reported that Y–BiOCl had higher photocatalytic activity than BiOCl, degrading 90.3 % of tetracycline [18]. Additionally, Y-doping narrowed the bandgap of BiOCl, which reduced the rate of photocarrier recombination and increased the photocatalytic activity [18]. In another study, Li et al. mentioned that Zn-doped BiOCl degraded 100 % of RhB dye under visible light irradiation [9]. It is reported that the improved photocatalytic activity is mainly attributed to high BET surface area and effective separation of photogenerated electron-hole pairs of the samples [9]. Composite formation is also a favorable modification to help enhance the photocatalytic activity [20,21]. For example, Anwar et al. fabricated Ag@BiOCl/g-C_3N_4 composite and the photocatalytic activities were greater than BiOCl. The Ag@BiOCl/g-C_3N_4 composite degraded about 92 % and 95.29 % of RhB and Crystal Violet, respectively [20].

In this work, doping BiOCl with tin (Sn) is a promising approach for enhancing photocatalytic activity under visible light irradiation. BiOCl and Sn-doped BiOCl were fabricated using a one-step co-precipitation method at ambient conditions. To the best of our knowledge, the photocatalytic degradation of RhB dye using visible light as a light source for Sn-doped BiOCl that was synthesized using the co-precipitation method has not been reported yet. Moreover, the photoelectrochemical studies on Sn-doped BiOCl such as linear sweep voltammetry (LSV) and electrochemical impedance spectroscopy (EIS) conducted in the dark and under visible light irradiation, have also not yet been reported. Several characterization techniques were used to determine the phase, structure, morphology, and optical properties of the as-synthesized materials. Therefore, the aim of this research is to investigate the effect of Sn as a dopant on the photocatalytic activity of the BiOCl under visible light irradiation. Furthermore, photoelectrochemical studies using methods like LSV and EIS were also carried out to understand the visible-light-induced response.

2. Experimental method

2.1. Materials

Bismuth nitrate pentahydrate ($Bi(NO_3)_3{\cdot}5H_2O$, 97 %) was acquired from VWR, USA. Potassium chloride (KCl) was purchased from BDH, UK. Tin (IV) chloride pentahydrate ($SnCl_4{\cdot}5H_2O$, 98 %), ethylene glycol ($(CH_2OH)_2$, 99.8 %), and ethyl cellulose (48.0–49.5 % (w/w) ethoxy basis) were obtained from Sigma Aldrich, Germany. Alpha-terpineol (α-terpineol) was obtained from Merck, Germany. Ethanol (C_2H_5OH, 95 %) was acquired from Daejung Chemicals and Metals Co. Ltd., South Korea. Sodium sulfite anhydrous (Na_2SO_3) was acquired from Fisher Scientific, USA. Double distilled was purified using Aquatron, England, and was used throughout the experiment.

2.2. Synthesis of BiOCl and Sn-doped BiOCl

For the preparation of BiOCl, Bi solution was first prepared by dissolving 0.80 M of $Bi(NO_3)_3{\cdot}5H_2O$ in ethylene glycol. The solution was stirred for 20 min. The next step was to prepare a 0.80 M aqueous solution of KCl. The KCl solution was added to the prepared Bi solution after 20 min. Subsequently, the mixture was rapidly agitated for 1 h at room temperature. The white product was then separated using centrifugation. The product was washed with ethanol and water for three times to remove impurities. The solid was ground using an agate mortar and pestle after drying at 80 °C. The finished product was a fine white powder.

For the synthesis of Sn-doped BiOCl, a desired amount (1 %, 5 %, and 10 %) of $SnCl_4{\cdot}5H_2O$ and 0.8 mmol of $Bi(NO_3)_3{\cdot}5H_2O$ were dissolved in 9.60 mL of double-distilled water and magnetically stirred for 20 min. The mixture was then added to 0.8 mmol of KCl solution and rapidly stirred for 1 h. The product was separated using centrifugation. The product was then rinsed with ethanol and water three times. The materials were crushed into fine powders using an agate mortar and pestle after drying at 80 °C. The desired amounts of Sn-doped BiOCl prepared were 1 %, 5 %, and 10 % and denoted as 1 % SBCl, 5 % SBCl, and 10 % SBCl, respectively.

2.3. Characterization

A series of techniques were used for the characterization of the as-synthesized BiOCl and SBCl. Powder X-ray diffraction (XRD) was carried out with a Rigaku MiniFlex ($\lambda = 1.5406$ Å) at a scan rate of 2° min^{-1} to determine the crystal phase structure. The samples were examined at a 2θ value between 20 and 80°. Fourier Transform Infrared Spectroscopy (FT-IR, Shimadzu IRSpirit) was used to investigate associated vibrational modes present in the synthesized materials. Raman analysis (DXR, Thermo Scientific) was performed with an excitation wavelength of 255 nm (laser power of 2.5 mW) to obtain the details on the chemical structures. UV–visible diffuse reflectance spectroscopy (UV–Vis DRS, Shimadzu UV 2600) was employed to measure the absorption, band structures, and overall optical properties. Photoluminescence spectroscopy (PL) was carried out using a Jasco FP-8500ST fluorescence spectrophotometer. JEOL JEM 2100 instrument was utilized for Transmission electron microscopy (TEM) and high-resolution transmission electron microscopy (HRTEM) analysis to study the surface morphology and particle size. N_2 adsorption and desorption isotherms were conducted using the ASAP 2020 torsimeter (Micrometric). The Brunauer Emmett-Teller (BET) method is used to determine the specific surface areas. The photoelectrochemical studies were carried out in the dark and under visible light irradiation (Simon FL30 LED Floodlight, Jiangsu, China) and were measured using a potentiostat Autolab (MetroHm, Herisau, Switzerland). A TOPTION V photoreactor equipped with a 300 W Xenon lamp was used to perform the photocatalytic process of the photocatalysts. The UV–visible spectroscopy (UV–Vis, Shimadzu UV-1900) was used to evaluate the photocatalytic degradation of RhB dye.

2.4. Photoelectrochemical studies of BiOCl and Sn-doped BiOCl

The working electrodes for LSV and EIS were fabricated by sonicating 25 mg of each sample for 10 min in 500 μL of ethanol and α-terpineol for full dispersion. After that, 25 mg of ethyl cellulose was then added as a binder to the sonicated mixture. To produce a thick paste, the mixture was heated to 80 °C and magnetically agitated for 1 h. The paste was coated on the fluorine-doped tin oxide (FTO) glass electrode by 2 cm × 1 cm using the doctor-blade technique. A potentiostat with a three-electrode system was used to record the LSV and EIS measurements. The three-electrode system includes BiOCl and SBCl (coated on FTO glass), Pt sheet, and Ag/AgCl as the working electrode, counter electrode, and reference electrode, respectively. At ambient conditions, the LSV and EIS studies of BiOCl and SBCl were carried out in 80 mL of 0.1 M Na_2SO_3 aqueous solution in the dark and in the presence of visible light. The LSV was measured at a scan rate of 50 mVs^{-1} with a potential range of −0.8 to 1.2 V. The EIS was studied at the frequency range of $1–10^5$ Hz and at a potential of 0.55 V.

2.5. Photocatalytic dye degradation of BiOCl and Sn-doped BiOCl

RhB dye was employed as the target pollutant to evaluate the photocatalytic performance of BiOCl and SBCl under visible light irradiation. Generally, 20 mg of the photocatalyst was dispersed into the 50 mL of 10 ppm RhB aqueous solution. Before the photocatalytic reaction, the suspension was sonicated for 10 min and agitated in the dark for 30 min to achieve adsorption-desorption equilibrium. Subsequently, the photocatalytic reaction was run for 1 h while being exposed to visible light. Every 10 min, 3 mL of the suspension was taken out and centrifuged to separate the photocatalyst. After that, the photocatalytic degradation efficiency of BiOCl and SBCl was analyzed using a UV–vis spectrophotometer by measuring the absorbance between the wavelengths of 200–800 nm.

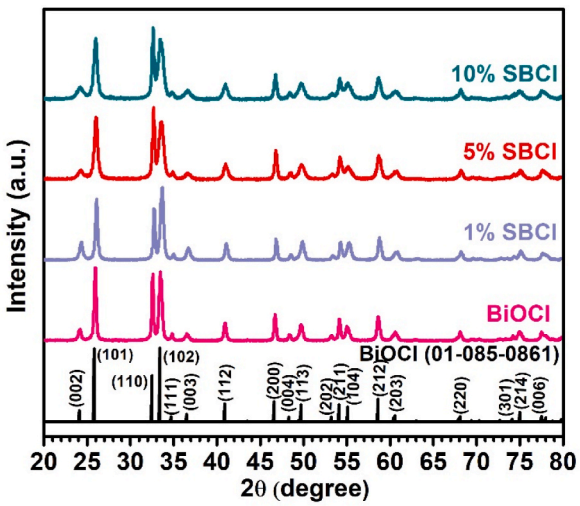

Fig. 1. The powder XRD patterns of the as-prepared BiOCl, 1 %, 5 %, and 10 % SBCl.

3. Results and discussion

3.1. Powder XRD analysis

The crystal structure of BiOCl, 1 %, 5 %, and 10 % SBCl was examined using powder XRD technique. The diffraction peaks of BiOCl and SBCl samples were indexed to the tetragonal crystal of BiOCl (JCPDS no. 1-085-0861) as shown in Fig. 1 [23]. There are no additional peaks indicating the absence of impurities. The three major crystal planes were observed at 25.91°, 32.57°, and 33.46° which are assigned to the (101), (110), and (102) planes, respectively. The peak ratio between the (110) and (102) planes in the BiOCl standard is 0.63. The as-prepared BiOCl, 1 % SBCl, 5 % SBCl, and 10 % SBCl all have peak ratios of 0.97, 0.34, 1.02, and 1.02, respectively. The samples have preferential growth in the [110] direction when a doping dosage of Sn increased, as seen by the diffraction peak ratio of (110) over (102). In addition, the crystallite sizes of BiOCl, 1 % SBCl, 5 % SBCl, and 10 % SBCl were determined using the Debye-Scherrer equation provided in **equation (1)**,

$$D = \frac{K\lambda}{\beta \cos\theta} \tag{1}$$

where D is crystallite size, β = FWHM (Full width at half maximum) at θ peak, λ = X-ray wavelength used, θ = Bragg angle, and $K = 0.9$.

The average crystallite size of BiOCl, 1 %, 5 %, and 10 % SBCl were 34.60, 29.15, 21.73, and 20.12 nm, respectively. It is evident that as the concentration of Sn increases, the crystallite size decreases. This might be due to the increase of Sn doping and reduced Bi concentration in the system [24]. However, there is only a minor change in the lattice parameters and unit cell volume of the BiOCl due to the Sn doping. Moreover, other structural parameters such as lattice strain were also determined. The calculated lattice parameters, unit cell volume, mean crystallite size, and the average lattice strain of the BiOCl, 1 %, 5 %, and 10 % SBCl are shown in Table 1 [24]. It was observed that the value of the average lattice strain increased progressively when 1 %, 5 %, and 10 % Sn were incorporated. Furthermore, there is a slight increase in the cell volume as more Sn was doped from 1 % to 10 %. Overall, this result suggests that Sn was successfully incorporated into the BiOCl lattice.

3.2. FT-IR analysis

FT-IR spectroscopy was carried out in the range of 4000-400 cm^{-1} to determine the related vibrational modes of the as-prepared materials. In Fig. 2(a), a broad peak was seen at 3424 cm^{-1}, which is caused by the OH stretching vibration of adsorbed H_2O species [4]. The bending vibrations of H_2O species that had been adsorbed produced the peaks at 1623 cm^{-1}. The weak peaks at 1382 cm^{-1} were attributed to the Bi–Cl band. The Bi–O band was said to be responsible for the intense peak at 524 cm^{-1}. Additionally, compared to BiOCl, 1 % SBCl, and 10 % SBCl, the 5 % SBCl had more adsorbed H_2O species [4]. Similar findings were reported in other studies. For instance, Yu et al. conducted the FT-IR analysis of Mn-doped BiOCl. The peaks observed at 525 cm^{-1} and 1623 cm^{-1} were assigned to Bi–O and adsorbed OH bands, respectively [25]. In another study, Han et al. synthesized Sn-doped BiOCl via a co-precipitation method with controlled pH. They reported two FT-IR peaks at around 533 cm^{-1} and 1616 cm^{-1} for Bi–O and OH bands, respectively [26]. In this study, it was observed that as the Sn content increases, the peak intensity at 524 cm^{-1} weakens. This could be due to the decrease in the Bi–O content [27]. This FT-IR result is in agreement with the XRD analysis, in which the Sn dopant was successfully introduced into the BiOCl lattice.

3.3. Raman analysis

Fig. 2(b) shows the Raman spectra of BiOCl, 1 % SBCl, 5 % SBCl, and 10 % SBCl. There were three vibrational peaks observed for each sample. The strongest peak is at around 144 cm^{-1} and was assigned to the A_{1g} mode, which refers to the internal Bi–Cl stretching mode. The next peak located around 210 cm^{-1} was due to the Bi–Cl bands with E_g stretching mode. The weakest peak at around 398 cm^{-1} was caused by the vibrations of Bi–O atoms with E_g/B_g stretching modes [28,29]. These three peaks are typically observed and reported for BiOCl in the literature [12,29]. For instance, Jiang et al. synthesized BiOCl and sulfur-doped BiOCl using a solvothermal technique. The author performed Raman analysis and found three distinguishable peaks at 141, 199, and 397 cm^{-1} [12]. In another report, Mi et al. investigated the Raman spectra of Fe-doped BiOCl and the results also showed three distinct peaks at 143.7 cm^{-1}, 198.2 cm^{-1}, and 395.9 cm^{-1} [29]. This result suggests that there are no additional peaks present in 1 %, 5 %, and 10 % SBCl due to the Sn doping, which is in accordance with the XRD analysis.

Table 1
Lattice parameters, unit cell volume, mean crystallite size, and average lattice strain of the as-synthesized BiOCl, 1 % SBCl, 5 % SBCl, and 10 % SBCl.

Samples	Lattice parameters (Å)		Unit cell volume (Å^3)	Mean crystallite size (nm)	Average lattice strain (ε)
	a	c			
BiOCl	3.885	7.371	111.26	34.60	0.0011
1 % SBCl	3.869	7.319	109.54	29.15	0.0013
5 % SBCl	3.876	7.343	110.30	21.73	0.0019
10 % SBCl	3.882	7.354	110.83	20.12	0.0021

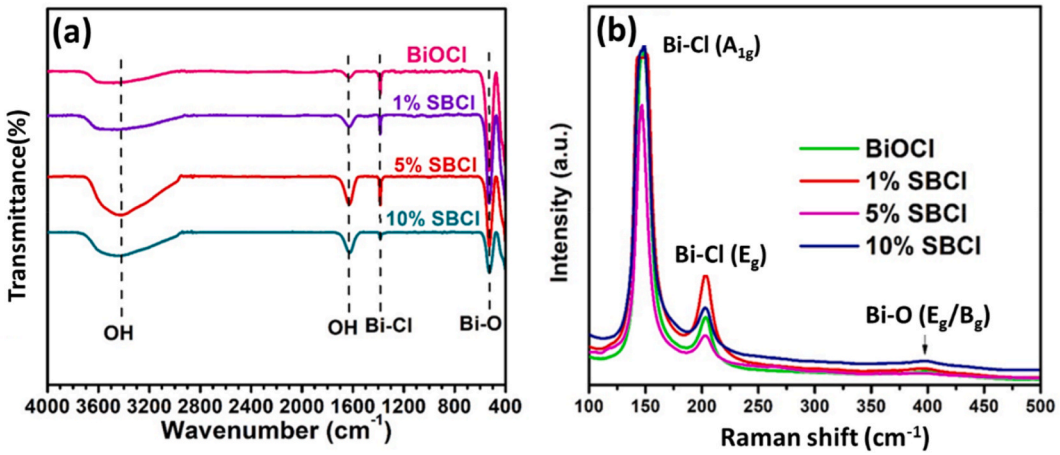

Fig. 2. **(a)** FT-IR and **(b)** Raman spectra of BiOCl, 1 % SBCl, 5 % SBCl, and 10 % SBCl.

3.4. UV–vis DRS analysis

In Fig. 3(a), the UV–Vis DRS spectra of BiOCl, 1 %, 5 %, and 10 % SBCl are shown. It was observed that the absorbance spectra (inset in Fig. 3(a)) of all the samples exhibit high absorbance in the UV region. In addition, the inset also shows the colour of the BiOCl, 1 % SBCl, 5 % SBCl, and 10 % SBCl. It is apparent that the colour changes from white to pale yellow, as the Sn dopant increases. Moreover, the band gap energy of BiOCl, 1 %, 5 %, and 10 % SBCl was evaluated using the Kubelka-Munk method. The band gap energy was determined by the intercept of the extrapolated linear part of the plot at $[F(R)h\nu]^{1/2} = 0$. The obtained band gap energy of BiOCl, 1 % SBCl, 5 % SBCl, and 10 % SBCl were 3.40 eV, 3.37 eV, 3.34 eV, and 3.36 eV, respectively. Similar values were reported in previous studies. Guan et al. examined the band gap energy of Sn-doped BiOCl nanoflowers synthesized using a solvothermal method to be about 3.25 eV. The author mentioned that the addition of Sn did not assist in the narrowing of the band gap [30]. In another study, Li et al. fabricated Zn-doped BiOCl via a solvothermal route. The band gap was determined to be 3.37 eV [9]. Based on this result, it can be suggested that the increase in Sn dopant has little effect on the absorption edge and the band gap tuning.

3.5. PL characterization

Generally, PL analysis is used to investigate the electron-hole recombination or separation processes in semiconductors and study the surface defects as well [31]. The PL spectra of BiOCl, 1 %, 5 %, and 10 % SBCl were measured over a wavelength range between 300 and 650 nm by an excitation source of 255 nm as shown in Fig. 3(b). For each sample, it was observed that there was a minimal change in the peak positions. Moreover, the emission intensity was enhanced after the addition of Sn dopant. This could be attributed to the oxygen vacancies and defects that might be present in SBCl [32,33]. Generally, the PL signal is dependent on the particle size and the amount of oxygen vacancy. The smaller the particle size, the higher the content of oxygen vacancy, and the greater the likelihood of

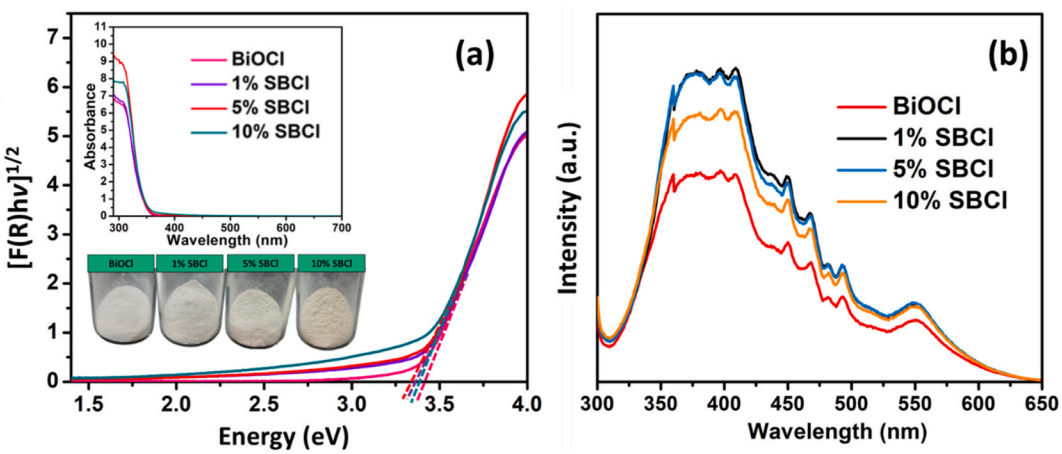

Fig. 3. **(a)** Tauc plots constructed from Kubelka-Munk transformed diffuse reflectance and **(b)** PL spectra of BiOCl, 1 % SBCl, 5 % SBCl, and 10 % SBCl. Inset in Fig. 3(a) shows the plot of -log reflectance (i.e. absorbance) and the sample colour of all the as-synthesized materials. (For interpretation of the references to colour in this figure legend, the reader is referred to the Web version of this article.)

exciton formation. Thus, the more enhanced the PL intensity [34]. In addition, the excitation wavelength used was 255 nm which was lower than the band gap obtained for BiOCl and SBCl samples. Therefore, the PL emission might be caused by the electron transitions related to surface defects or surface state energy levels other than the electron transitions between the conduction band and valence band [33–35]. This result suggests that the optical property of 1 %, 5 %, and 10 % SBCl was improved by the successful incorporation of Sn and might have formed oxygen vacancies or surface defects.

3.6. TEM analysis

Fig. 4 displays the TEM, HRTEM, and selected area electron diffraction (SAED) patterns of BiOCl and 5 % SBCl only. It can be seen from the TEM images of BiOCl (Fig. 4(a)) and 5 % SBCl (Fig. 4(d)) that both possessed an irregular nanoplate-like morphology. Moreover, the average thickness of BiOCl and 5 % SBCl is about 16 nm and 9 nm, respectively. The decrease in thickness could suggest that the Sn is successfully incorporated into the BiOCl lattice. The HRTEM images of BiOCl (Fig. 4(b)) and 5 % SBCl (Fig. 4(e)) show clear lattice fringes, exhibiting good crystallinity. Furthermore, the d-spacing value of the lattice planes was also determined. The d-spacing values for BiOCl and 5 % SBCl (**inset in Fig. 4(b), (e)**) were estimated to be around 0.376 nm and 0.330 nm, which corresponds to the (002), and (101) planes of the tetragonal structure of BiOCl, respectively [36]. Furthermore, the crystallinity of BiOCl and 5 % SBCl was further confirmed using SAED analysis. It can be seen that BiOCl (Fig. 4(c)) and 5 % SBCl (Fig. 4(f)) displayed four broad and clear rings, which can be attributed to the (002), (101), (110), and (102) reflections of the tetragonal BiOCl structure. Similar findings can be found in other reported studies. For instance, Zhong et al. synthesized Fe-doped BiOCl and estimated the lattice spacing to be about 0.371 nm which corresponds to the (002) plane of BiOCl [37]. These results are in accordance with the XRD findings and confirm the successful synthesis of BiOCl and Sn-doped BiOCl.

3.7. BET analysis

In order to acquire the specific surface area and determine the type of isotherm of the as-prepared BiOCl, 1 %, 5 %, and 10 % SBCl, the N_2 adsorption–desorption isotherm measurements were carried out. Fig. 5 shows the N_2 adsorption–desorption isotherms plot of BiOCl, 1 % SBCl, 5 % SBCl, and 10 % SBCl. The inset shows the zoom area of the relative pressure between the range of 0.84–1.02. It was observed that all of the as-synthesized samples exhibit a type-IV isotherm containing an H3 hysteresis loop, which indicates the presence of mesoporous structure [38].

The specific surface area of these samples was measured using the BET method and is shown in Table 2. In comparison to BiOCl, it can be seen that the SBCl samples have a higher specific surface area. The specific surface area increases from 13.49 to 42.20 m^2/g. It is clear that with the increase of Sn doping, the specific surface area significantly increases. It is widely known that the surface area has a significant impact on the photocatalytic activity. A greater BET surface area can result in more active sites on the catalyst surface, which can improve photocatalytic activity [9,39]. Furthermore, because of the larger surface area of SBCl, the dye can be transported and diffused through the pores and surfaces, which helps to improve SBCl photocatalytic efficacy [40]. Therefore, it can be concluded that the increase in specific surface area was attributed to the successful incorporation of Sn into the BiOCl lattice, in which the Sn doping produces more active sites. Hence, it helps to improve the photocatalytic performance of BiOCl.

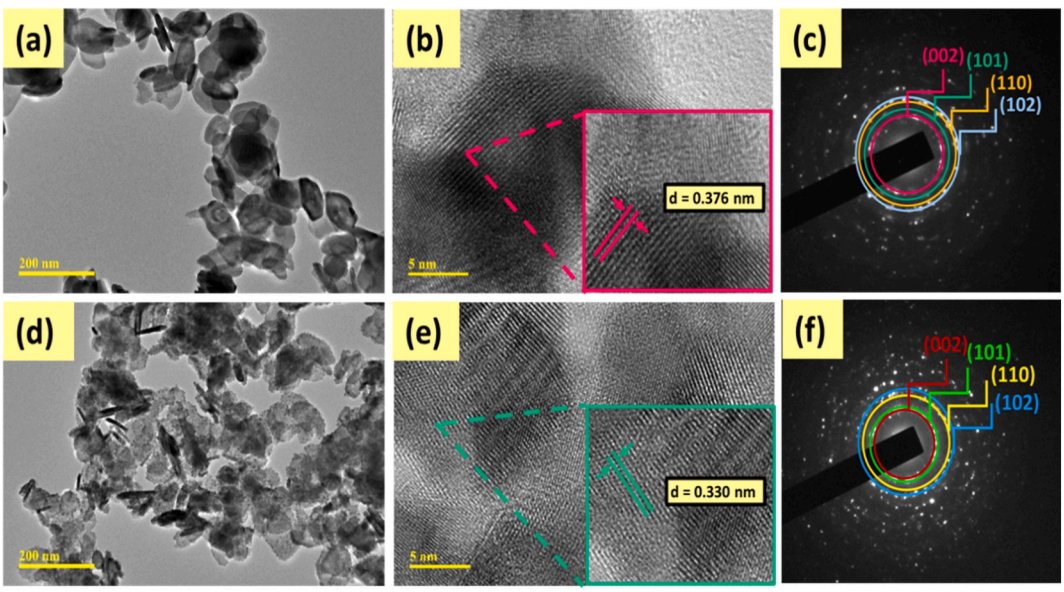

Fig. 4. TEM, HRTEM, and SAED patterns of **(a–c)** BiOCl and **(d–f)** 5 % SBCl. Inset in Fig. 4(b) and (e) are the zoom sections of the HRTEM images of BiOCl and 5 % SBCl, respectively.

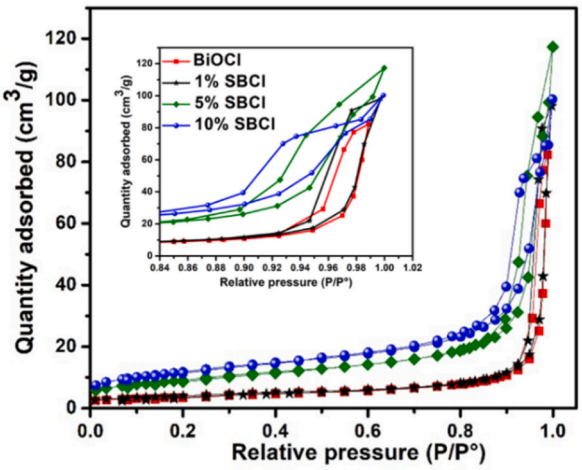

Fig. 5. N_2 gas adsorption-desorption isotherms of BiOCl, 1 %, 5 %, and 10 % SBCl photocatalysts (inset: the zoom region of relative pressure between 0.84 and 1.02).

Table 2
The obtained specific surface area of BiOCl, 1 %, 5 %, and 10 % SBCl.

Samples	BET surface area (m^2/g)
BiOCl	13.49
1 % SBCl	14.66
5 % SBCl	33.12
10 % SBCl	42.20

4. Photoelectrochemical studies of BiOCl and Sn-doped BiOCl

LSV is a technique that measures the current at a working electrode while linearly varying the voltage between the working electrode and a reference electrode [41,42]. To investigate the photoactivity of BiOCl, 1 %, 5 %, and 10 % SBCl, LSV was carried out in the dark and under visible light irradiation. Fig. 6(a) and Fig. 6(b) demonstrate the overall trend for measuring the current in the dark and under visible light irradiation, respectively. Moreover, all of the samples responded with a higher current when exposed to visible light than when they were in the dark. As shown in Fig. 6(a), it was observed that 1 %, 5 %, and 10 % SBCl displayed higher current than BiOCl in the dark. Among the samples, 5 % SBCl has the highest current of 0.53 mA. Fig. 6(b) shows the LSV measurements carried out under visible light irradiation. It can be seen that the 1 %, 5 %, and 10 % SBCl exhibited better photocurrent performance than BiOCl. A high photocurrent typically indicates that the sample has a strong capacity for producing and transporting the photoinduced charge carriers when exposed to light [43,44]. The highest photocurrent recorded was for 5 % SBCl with a value of 0.61 mA, which is higher than the current in the dark. The enhancement in photocurrent infers that it may be easily stimulated by visible light and produce more photoinduced charge carriers, which might lead to higher visible-light-induced photocatalytic activity [43,44].

To comprehend the charge separation process and transport properties, EIS was measured. The obtained Nyquist plot of BiOCl, 1 %, 5 %, and 10 % SBCl in the dark and under visible light irradiation was shown in Fig. 6(c) and (d), respectively. The EIS results showed that all of the SBCl samples carried out in the dark and under visible light irradiation have a smaller arc radius compared to BiOCl. Furthermore, it can be seen that 5 % SBCl has the smallest arc radius in the dark and under visible light irradiation. It is expected that the arc radius would be smaller when measured under visible light irradiation than in dark. This indicates a faster electron transfer in the presence of light than in the dark. Therefore, the smaller arc radius corresponds to a lower electron transfer resistance at the photoelectrode surface, which is frequently linked to a fast interfacial charge transfer [42]. Overall, it can be suggested that Sn doping can accelerate the transfer of electrons and as a result, assist in improving the separation efficiency of photoinduced electron-hole pairs of SBCl at 1 %, 5 %, and 10 % [45,46]. These findings are in agreement with photocatalytic studies where 5 % SBCl has the highest photocatalytic efficiency in degrading RhB dye.

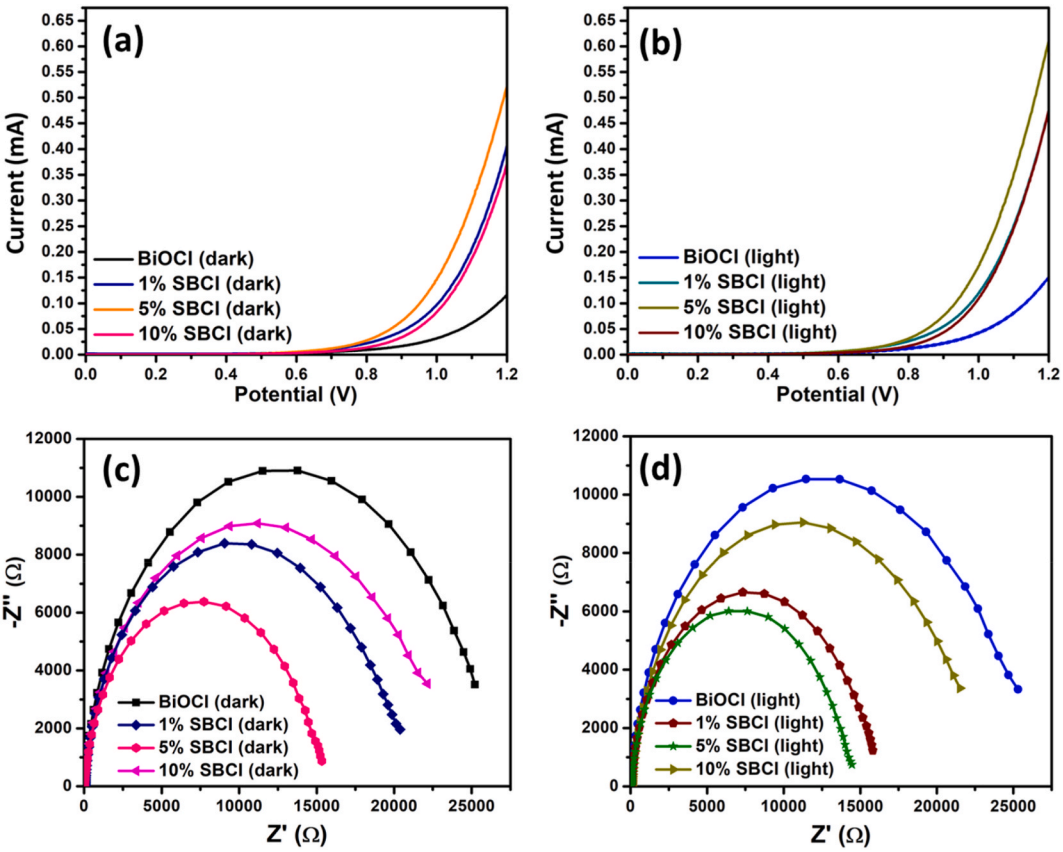

Fig. 6. **(a–b)** LSV plots with a scan rate of 50 mVs^{-1} and **(c–d)** Nyquist plots of BiOCl, 1 %, 5 %, and 10 % SBCl in the dark and under visible light irradiation.

5. Photocatalytic studies of BiOCl and Sn-doped BiOCl

The photocatalytic performance of the synthesized materials was investigated using RhB dye as the model pollutant. The results of the photocatalytic degradation of RhB dye using BiOCl, 1 % SBCl, 5 % SBCl, and 10 % SBCl are shown in Fig. 7, where **(a)** is the kinetic analysis of photocatalytic degradation of RhB and **(b)** is the percentage of the photocatalytic degradation rate of each sample under visible light irradiation within 1 h. To evaluate the kinetic analysis and the photocatalytic efficiency of the as-prepared photocatalysts, the pseudo-first-order kinetics model in **equation (2)** was used. With respect to time 0 and t (min), C_0 and C_t are the concentrations of the RhB dye, respectively, and k (min^{-1}) is the pseudo-first-order rate constant.

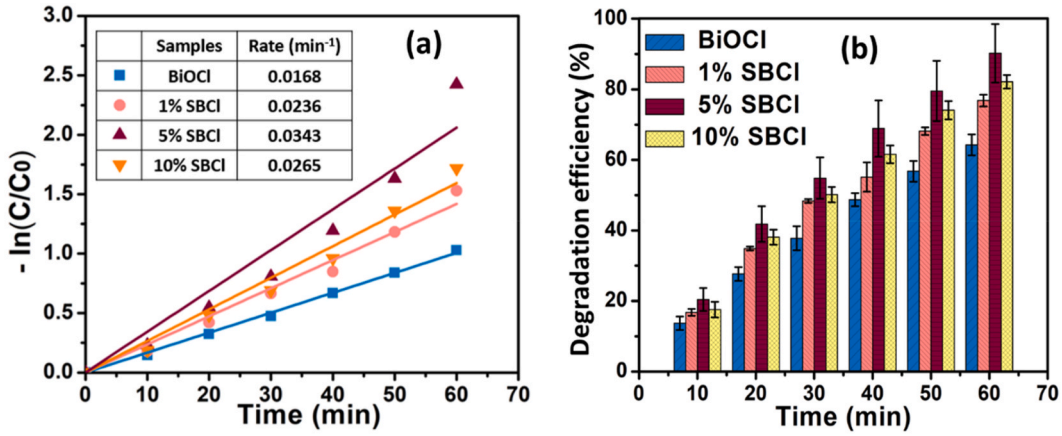

Fig. 7. **(a)** -ln(C/C_0), pseudo-first-order kinetics, and **(b)** RhB degradation efficiency of the as-prepared materials under visible light irradiation.

$$-\ln(C_t/C_0) = kt \quad (2)$$

According to the kinetic analysis displayed in Fig. 7(a), it was observed that the SBCl samples had a higher rate constant than BiOCl. Among the as-prepared samples, 5 % SBCl has the highest rate constant of 0.0343 min^{-1}. BiOCl has a rate constant of 0.0168 min^{-1} and the rate constant of 5 % SBCl is three times greater than that of BiOCl. Therefore, it can be deduced that the incorporation of Sn into the BiOCl lattice enhances the photocatalytic performance. Despite that, the photocatalytic rate starts to decrease as the concentration of Sn increase to 10 %. Although the 10 % SBCl has the largest specific surface area, this suggests that the optimum doping is at 5 %, and beyond that, it seemed to affect unfavorably on the photocatalytic activity. In Fig. 7(b), the photocatalytic degradation efficiency of BiOCl, 1 %, 5 %, and 10 % SBCl are shown. The photocatalytic removal of RhB dye using BiOCl, 1 %, 5 %, and 10 % SBCl is 64.3 %, 78.3 %, 91.2 %, and 82.1 %, respectively. This suggests that doping BiOCl with Sn helps enhance the photocatalytic performance. This might be attributed to the interdependent effect of large specific surface area and the rapid photogenerated electron–hole pair separation.

6. Conclusion

In summary, BiOCl and Sn-doped BiOCl were synthesized using the co-precipitation method at ambient conditions. The XRD studies determined the tetragonal phase of BiOCl, 1 % SBCl, 5 % SBCl, and 10 % SBCl. The mean crystallite sizes obtained were between 20 and 34 nm. This result can be further confirmed by FT-IR and Raman analysis. From BET evaluation, the specific surface area of BiOCl and 5 % SBCl are 13.49 m^2/g and 33.12 m^2/g, respectively. Among all of the as-prepared photocatalysts, 5 % SBCl has the highest photocatalytic activity, degrading 91.2 % of the RhB dye in 60 min whilst BiOCl only degraded about 64.3 %. The photocatalytic performance is in agreement with the photoelectrochemical studies, in which the photoelectrochemical activities of 5 % SBCl showed enhanced response under visible light irradiation. The high photocatalytic performance is attributed to the large specific surface area and rapid electron-hole separation of SBCl. It can be concluded that SBCl has shown visible light-responsive properties and can be potentially used as a photocatalyst and photoelectrode material.

Data availability statement

Data will be made available on request.

CRediT authorship contribution statement

Asyiqin Zulkiflee: Data curation, Formal analysis, Methodology, Writing – original draft. **Mohammad Mansoob Khan:** Conceptualization, Funding acquisition, Resources, Supervision, Writing – review & editing. **Abuzar Khan:** Formal analysis, Writing – review & editing. **Mohd Yusuf Khan:** Formal analysis, Writing – review & editing. **Hatim Dafalla Mohamed Dafalla:** Formal analysis. **Mohammad Hilni Harunsani:** Conceptualization, Supervision, Writing – review & editing.

Declaration of competing interest

The authors declare that they have no known competing financial interests or personal relationships that could have appeared to influence the work reported in this paper.

Acknowledgement

This research was funded by Universiti Brunei Darussalam through grant UBD/RSCH/1.4/FICBF(b)/2021/035. The authors would like to express gratitude to Mohd Yusuf Khan and Abuzar Khan from the Interdisciplinary Research Center for Hydrogen and Energy Storage, King Fahd University of Petroleum & Minerals (KFUPM), Dhahran, 31261, Saudi Arabia for the research support.

References

[1] M.M. Khan, S.F. Adil, A. Al-Mayouf, Metal oxides as photocatalysts, J. Saudi Chem. Soc. 19 (2015) 462–464, https://doi.org/10.1016/j.jscs.2015.04.003.
[2] A. Rahman, M.M. Khan, Chalcogenides as photocatalysts, New J. Chem. 45 (2021) 19622–19635, https://doi.org/10.1039/D1NJ04346C.
[3] M.M. Khan, S.A. Ansari, D. Pradhan, M.O. Ansari, D.H. Han, J. Lee, M.H. Cho, Band gap engineered TiO_2 nanoparticles for visible light induced photoelectrochemical and photocatalytic studies, J. Mater. Chem. A 2 (2014) 637–644, https://doi.org/10.1039/C3TA14052K.
[4] Y.I. Choi, K.H. Jeon, H.S. Kim, J.H. Lee, S.J. Park, J.E. Roh, M.M. Khan, Y. Sohn, TiO_2/BiOX (X=Cl, Br, I) hybrid microspheres for artificial waste water and real sample treatment under visible light irradiation, Sep. Purif. Technol. 160 (2016) 28–42, https://doi.org/10.1016/j.seppur.2016.01.009.
[5] J. Yuan, J. Wang, Y. She, J. Hu, P. Tao, F. Lv, Z. Lu, Y. Gu, BiOCl micro-assembles consisting of ultrafine nanoplates: a high performance electro-catalyst for air electrode of Al–air batteries, J. Power Sources 263 (2014) 37–45, https://doi.org/10.1016/j.jpowsour.2014.04.022.
[6] M.M. Khan, Theoretical Concepts of Photocatalysis, Elsevier, 2023, https://doi.org/10.1016/C2021-0-01798-3.
[7] M.M. Khan, Introduction and fundamentals of chalcogenides and chalcogenides-based nanomaterials, in: Chalcogenide-Based Nanomater. As Photocatal, Elsevier, 2021, pp. 1–6, https://doi.org/10.1016/B978-0-12-820498-6.00001-9.
[8] X. Lv, F.L.Y. Lam, X. Hu, A review on bismuth oxyhalide (BiOX, X=Cl, Br, I) based photocatalysts for wastewater remediation, Front. Catal. 2 (2022) 1–24, https://doi.org/10.3389/fctls.2022.839072.
[9] W.T. Li, W.Z. Huang, H. Zhou, H.Y. Yin, Y.F. Zheng, X.C. Song, Synthesis of Zn^{2+} doped BiOCl hierarchical nanostructures and their exceptional visible light photocatalytic properties, J. Alloys Compd. 638 (2015) 148–154, https://doi.org/10.1016/j.jallcom.2015.03.103.

[10] L. Ye, J. Liu, C. Gong, L. Tian, T. Peng, L. Zan, Two different roles of metallic Ag on Ag/AgX/BiOX (X = Cl, Br) visible light photocatalysts: surface plasmon resonance and Z-scheme bridge, ACS Catal. 2 (2012) 1677–1683, https://doi.org/10.1021/cs300213m.

[11] A. Zulkiflee, M.M. Khan, M.H. Harunsani, Bismuth oxyhalides: recent progress and its applications in photocatalysis, hydrogen production, antibacterial studies, and sensors, Mater. Sci. Semicond. Process. 163 (2023), 107547, https://doi.org/10.1016/j.mssp.2023.107547.

[12] Z. Jiang, Y. Liu, T. Jing, B. Huang, Z. Wang, X. Zhang, X. Qin, Y. Dai, One-pot solvothermal synthesis of S doped BiOCl for solar water oxidation, RSC Adv. 5 (2015) 47261–47264, https://doi.org/10.1039/c5ra07776a.

[13] C.-Y. Wang, Y.-J. Zhang, W.-K. Wang, D.-N. Pei, G.-X. Huang, J.-J. Chen, X. Zhang, H.-Q. Yu, Enhanced photocatalytic degradation of bisphenol A by Co-doped BiOCl nanosheets under visible light irradiation, Appl. Catal. B Environ. 221 (2018) 320–328, https://doi.org/10.1016/j.apcatb.2017.09.036.

[14] J. Li, Y. Yu, L. Zhang, Bismuth oxyhalide nanomaterials: layered structures meet photocatalysis, Nanoscale 6 (2014) 8473–8488, https://doi.org/10.1039/C4NR02553A.

[15] L. Sun, L. Xiang, X. Zhao, C.J. Jia, J. Yang, Z. Jin, X. Cheng, W. Fan, Enhanced visible-light photocatalytic activity of bioi/biocl heterojunctions: key role of crystal facet combination, ACS Catal. 5 (2015) 3540–3551, https://doi.org/10.1021/cs501631n.

[16] A.M. Ganose, M. Cuff, K.T. Butler, A. Walsh, D.O. Scanlon, Interplay of orbital and relativistic effects in bismuth oxyhalides: BiOF, BiOCl, BiOBr, and BiOI, Chem. Mater. 28 (2016) 1980–1984, https://doi.org/10.1021/acs.chemmater.6b00349.

[17] P. Yan, L. Xu, J. Xia, Y. Huang, J. Qiu, Q. Xu, Q. Zhang, H. Li, Photoelectrochemical sensing of 4-chlorophenol based on Au/BiOCl nanocomposites, Talanta 156–157 (2016) 257–264, https://doi.org/10.1016/j.talanta.2016.05.004.

[18] S. Zhong, X. Wang, Y. Wang, F. Zhou, J. Li, S. Liang, C. Li, Preparation of Y^{3+}-doped BiOCl photocatalyst and its enhancing effect on degradation of tetracycline hydrochloride wastewater, J. Alloys Compd. 843 (2020), 155598, https://doi.org/10.1016/j.jallcom.2020.155598.

[19] J. Liu, H. Wang, M.-J. Chang, M. Sun, C.-M. Zhang, L.-Q. Yang, H.-L. Du, Z.-M. Luo, Facile synthesis of BiOCl with extremely superior visible light photocatalytic activity synergistically enhanced by Co doping and oxygen vacancies, Sep. Purif. Technol. 301 (2022), 121953, https://doi.org/10.1016/j.seppur.2022.121953.

[20] M. Anwar, K.S. Alghamdi, S. Zulfiqar, M.F. Warsi, M. Waqas, M. Hasan, Ag-decorated BiOCl anchored onto the g-C_3N_4 sheets for boosted photocatalytic and antimicrobial activities, Opt. Mater. 135 (2023), 113336, https://doi.org/10.1016/j.optmat.2022.113336.

[21] T. Munawar, M.S. Nadeem, F. Mukhtar, M.N. ur Rehman, M. Riaz, S. Batool, M. Hasan, F. Iqbal, Transition metal-doped SnO_2 and graphene oxide (GO) supported nanocomposites as efficient photocatalysts and antibacterial agents, Environ. Sci. Pollut. Res. 29 (2022) 90995–91016, https://doi.org/10.1007/s11356-022-22144-3.

[22] A. Zulkiflee, M.M. Khan, M.Y. Khan, A. Khan, A.C. Ummer, M.H. Harunsani, Zirconium-doped BiOCl for enhanced visible light-induced photocatalytic degradation of RhB dye and photoelectrochemical studies, New J. Chem. 37 (2023), https://doi.org/10.1039/D3NJ02294C.

[23] Y.I. Choi, Y.-I. Kim, D.W. Cho, J.-S. Kang, K.T. Leung, Y. Sohn, Recyclable magnetic $CoFe_2O_4$/BiOX (X = Cl, Br and I) microflowers for photocatalytic treatment of water contaminated with methyl orange, rhodamine B, methylene blue, and a mixed dye, RSC Adv. 5 (2015) 79624–79634, https://doi.org/10.1039/C5RA17616F.

[24] N. Latha, Y.S. Vidya, S.C. Sharma, G.P. Darshan, K.S. Anantharaju, P.H. Prabha, H. Nagabhushana, Effect of Li^+ coodoping on the photoluminescence of novel green emitting BiOCl: Tb^{3+} nanophosphors for display, visualization of latent fingerprints and anticounterfeiting applications, J. Solid State Chem. 290 (2020), 121418, https://doi.org/10.1016/j.jssc.2020.121418.

[25] H. Yu, D. Ge, Y. Liu, Y. Lu, X. Wang, M. Huo, W. Qin, One-pot synthesis of BiOCl microflowers co-modified with Mn and oxygen vacancies for enhanced photocatalytic degradation of tetracycline under visible light, Sep. Purif. Technol. 251 (2020), 117414, https://doi.org/10.1016/j.seppur.2020.117414.

[26] X. Han, S. Dong, C. Yu, Y. Wang, K. Yang, J. Sun, Controllable synthesis of Sn-doped BiOCl for efficient photocatalytic degradation of mixed-dye wastewater under natural sunlight irradiation, J. Alloys Compd. 685 (2016) 997–1007, https://doi.org/10.1016/j.jallcom.2016.06.298.

[27] Y. Deng, M. Xu, X. Jiang, J. Wang, P.-L. Tremblay, T. Zhang, Versatile iodine-doped BiOCl with abundant oxygen vacancies and (110) crystal planes for enhanced pollutant photodegradation, Environ. Res. 216 (2023), 114808, https://doi.org/10.1016/j.envres.2022.114808.

[28] W.J. Kim, D. Pradhan, B.-K. Min, Y. Sohn, Adsorption/photocatalytic activity and fundamental natures of BiOCl and $BiOCl_xI_{1-x}$ prepared in water and ethylene glycol environments, and Ag and Au-doping effects, Appl. Catal. B Environ. 147 (2014) 711–725, https://doi.org/10.1016/j.apcatb.2013.10.008.

[29] Y. Mi, L. Wen, Z. Wang, D. Cao, R. Xu, Y. Fang, Y. Zhou, Y. Lei, Fe(III) modified BiOCl ultrathin nanosheet towards high-efficient visible-light photocatalyst, Nano Energy 30 (2016) 109–117, https://doi.org/10.1016/j.nanoen.2016.10.001.

[30] C. Guan, T. Hou, W. Nie, Q. Zhang, L. Duan, X. Zhao, Sn^{4+} doping enhanced inner electric field for photocatalytic performance promotion of BiOCl based nanoflowers, Appl. Surf. Sci. 604 (2022), 154498, https://doi.org/10.1016/j.apsusc.2022.154498.

[31] K. Anandan, V. Rajendran, Studies on structural, morphological, magnetic and optical properties of chromium sesquioxide (Cr_2O_3) nanoparticles: synthesized via facile solvothermal process by different solvents, Mater. Sci. Semicond. Process. 19 (2014) 136–144, https://doi.org/10.1016/j.mssp.2013.12.004.

[32] R. Mani, K. Vivekanandan, K. Vallalperuman, Synthesis of pure and cobalt (Co) doped SnO_2 nanoparticles and its structural, optical and photocatalytic properties, J. Mater. Sci. Mater. Electron. 28 (2017) 4396–4402, https://doi.org/10.1007/s10854-016-6067-z.

[33] J. Liqiang, Q. Yichun, W. Baiqi, L. Shudan, J. Baojiang, Y. Libin, F. Wei, F. Honggang, S. Jiazhong, Review of photoluminescence performance of nano-sized semiconductor materials and its relationships with photocatalytic activity, Sol. Energy Mater. Sol. Cells 90 (2006) 1773–1787, https://doi.org/10.1016/j.solmat.2005.11.007.

[34] J. Liqiang, S. Xiaojun, X. Baifu, W. Baiqi, C. Weimin, F. Honggang, The preparation and characterization of La doped TiO_2 nanoparticles and their photocatalytic activity, J. Solid State Chem. 177 (2004) 3375–3382, https://doi.org/10.1016/j.jssc.2004.05.064.

[35] W.F. Zhang, M.S. Zhang, Z. Yin, Q. Chen, Photoluminescence in anatase titanium dioxide nanocrystals, Appl. Phys. B Laser Opt. 70 (2000) 261–265, https://doi.org/10.1007/s003400050043.

[36] K.E. Ahmed, D.H. Kuo, L.W. Duresa, Synthesis and characterizations of BiOCl nanosheets with controlled particle growth for efficient organic dyes degradation, J. Ind. Eng. Chem. 83 (2020) 200–207, https://doi.org/10.1016/J.JIEC.2019.11.028.

[37] X. Zhong, K.-X. Zhang, D. Wu, X.-Y. Ye, W. Huang, B.-X. Zhou, Enhanced photocatalytic degradation of levofloxacin by Fe-doped BiOCl nanosheets under LED light irradiation, Chem. Eng. J. 383 (2020), 123148, https://doi.org/10.1016/j.cej.2019.123148.

[38] X. Gao, C. Gong, X. Wang, W. Zhu, Y. Luo, Facile synthesis of cobalt doped BiOCl ultrathin nanosheets as superior photocatalyst for degradation of carbamazepine under visible light, J. Solid State Chem. 298 (2021), 122131, https://doi.org/10.1016/j.jssc.2021.122131.

[39] Y.R. Yao, W.Z. Huang, H. Zhou, Y.F. Zheng, X.C. Song, Self-assembly of dandelion-like Fe_3O_4@C@BiOCl magnetic nanocomposites with excellent solar-driven photocatalytic properties, J. Nanoparticle Res. 16 (2014) 2451, https://doi.org/10.1007/s11051-014-2451-x.

[40] L. Shao, Y. Liu, L. Wang, X. Xia, X. Shen, Electronic structure tailoring of BiOBr (0 1 0) nanosheets by cobalt doping for enhanced visible-light photocatalytic activity, Appl. Surf. Sci. 502 (2020), 143895, https://doi.org/10.1016/j.apsusc.2019.143895.

[41] A. Yang, Y. Xue, Y. Zhang, X. Zhang, H. Zhao, X. Li, Y. He, Z. Yuan, A simple one-pot synthesis of graphene nanosheet/SnO_2 nanoparticle hybrid nanocomposites and their application for selective and sensitive electrochemical detection of dopamine, J. Mater. Chem. B 1 (2013) 1804, https://doi.org/10.1039/c3tb00513e.

[42] M.E. Khan, M.M. Khan, M.H. Cho, CdS-Graphene nanocomposite for efficient visible-light-driven photocatalytic and photoelectrochemical applications, J. Colloid Interface Sci. 482 (2016) 221–232, https://doi.org/10.1016/j.jcis.2016.07.070.

[43] S.A. Ansari, M.M. Khan, M.O. Ansari, S. Kalathil, J. Lee, M.H. Cho, Band gap engineering of CeO_2 nanostructure using an electrochemically active biofilm for visible light applications, RSC Adv. 4 (2014) 16782–16791, https://doi.org/10.1039/C4RA00861H.

[44] X. Lu, D. Zheng, P. Zhang, C. Liang, P. Liu, Y. Tong, Facile synthesis of free-standing CeO_2 nanorods for photoelectrochemical applications, Chem. Commun. 46 (2010) 7721, https://doi.org/10.1039/c0cc01854f.

[45] L. Xu, P. Yan, H. Li, S. Ling, J. Xia, J. Qiu, Q. Xu, H. Li, S. Yuan, Metallic Bi self-doping BiOCl composites: synthesis and enhanced photoelectrochemical performance, Mater. Lett. 196 (2017) 225–229, https://doi.org/10.1016/j.matlet.2017.03.008.

[46] J. Shang, B. Zhao, Y. Gao, H. Chen, X. Wang, Enhanced electricity generation in photoelectrochemical cell using Sn-doped BiOCl photoanode, J. Mater. Sci. Mater. Electron. 31 (2020) 13939–13946, https://doi.org/10.1007/s10854-020-03953-z.